

# Classification Study of DTI and HARDI Anisotropy Measures for HARDI Data Simplification

Vesna Prčkovska, Maxime Descoteaux, Cyril Poupon,  
Bart M. ter Haar Romeny, and Anna Vilanova

**Abstract** High angular resolution diffusion imaging (HARDI) captures the angular diffusion pattern of water molecules more accurately than diffusion tensor imaging (DTI). This is of importance mainly in areas of complex intra-voxel fiber configurations. However, the extra complexity of HARDI models has many disadvantages that make it unattractive for clinical applications. One of the main drawbacks is the long post-processing time for calculating the diffusion models. Also intuitive and fast visualization is not possible, and the memory requirements are far from modest. Separating the data into anisotropic-Gaussian (i.e., modeled by DTI) and non-Gaussian areas can alleviate some of the above mentioned issues, by using complex HARDI models only when necessary. This work presents a study of DTI and HARDI anisotropy measures applied as classification criteria for detecting non-Gaussian diffusion profiles. We quantify the classification power of these measures using a statistical test of receiver operation characteristic (ROC) curves applied on *ex-vivo* ground truth crossing phantoms. We show that some of the existing DTI and HARDI measures in the literature can be successfully applied for data

---

V. Prčkovska (✉)

Center for Neuroimmunology, Department of Neurosciences, Institut Biomedical Research August Pi Sunyer (IDIBAPS), Hospital Clinic of Barcelona, Spain  
e-mail: [VPRCHKOV@clinic.ub.es](mailto:VPRCHKOV@clinic.ub.es)

B.M. ter Haar Romeny · A. Vilanova

Department of Biomedical Engineering, Eindhoven University of Technology, Eindhoven, The Netherlands  
e-mail: [B.M.terHaarRomeny@tue.nl](mailto:B.M.terHaarRomeny@tue.nl); [A.Vilanova@tue.nl](mailto:A.Vilanova@tue.nl)

C. Poupon

NeuroSpin, CEA Saclay, Gif-sur-Yvette Cedex, France  
e-mail: [cyril.poupon@cea.fr](mailto:cyril.poupon@cea.fr)

M. Descoteaux

Computer science department, Université de Sherbrooke, Sherbrooke, QC, Canada  
e-mail: [m.descoteaux@usherbrooke.ca](mailto:m.descoteaux@usherbrooke.ca)

classification to the diffusion tensor or different HARDI models respectively. The chosen measures provide fast data classification that can enable data simplification. We also show that increasing the b-value and number of diffusion measurements above clinically accepted settings does not significantly improve the classification power of the measures. Moreover, we show that a denoising pre-processing step improves the classification. This denoising enables better quality classifications even with low b-values and low sampling schemes. Finally, the findings of this study are qualitatively illustrated on real diffusion data under different acquisition schemes.

## 1 Introduction

Diffusion tensor imaging (DTI) is a recent magnetic resonance imaging (MRI) technique that can map the orientation architecture of neural tissues in a completely non-invasive way by measuring the directional specificity (anisotropy) of local water diffusion [1]. The diffusion tensor model, however, has well known limitations in areas of complex intra-voxel heterogeneity with crossing fibers, where the diffusion process cannot be modeled as Gaussian. Nonetheless, DTI is still very popular and has many advantages such as fast and clinically feasible acquisition schemes (typically, number of gradients (NG) from 7 to 60, b-value of 1,000 s/mm<sup>2</sup> and total acquisition time of 3–5 min), fast post-processing of the data that allows interactivity in the data exploration, simple visualization techniques and modeling using well-developed tensor mathematics. To overcome the limitations of DTI, more sophisticated models were introduced using high angular resolution diffusion imaging (HARDI). For HARDI, significantly more diffusion gradients are acquired (from sixty to a several hundred) in order to reconstruct a spherical probability function (SPF) that either recovers the underlying fiber populations or depicts certain diffusion properties. Popular HARDI reconstruction techniques include apparent diffusion coefficient (ADC) modeling [2, 3], Q-Ball imaging [4], diffusion orientation transform (DOT) [5], spherical deconvolution (SD) [6, 7], and several other model-based methods. The output produced by the above techniques is always given in the form of a spherical function  $\psi(\theta, \phi)$  that characterizes the local intra-voxel fiber structure. This function can be represented using a truncated spherical harmonics (SH) expansion

$$\psi(\theta, \phi) = \sum_{l=0}^{l_{max}} \sum_{m=-l}^l a_{lm} Y_{lm}(\theta, \phi), \quad (1)$$

where  $Y_l^m$  represent the spherical harmonics of order  $l$  and phase  $m$ , and  $l_{max}$  is the truncation order of the SH series.

HARDI has obvious advantages over DTI in more composite fiber configurations, but has several drawbacks that accompany this complex modeling: longer processing time of the data (that can typically take a few hours up to a few days), inability to interactively explore the data because of over-cluttered and computationally heavy visualization as well as longer data acquisitions. Hence, one wonders if a complex high-order modeling of the data is always needed (i.e., at every

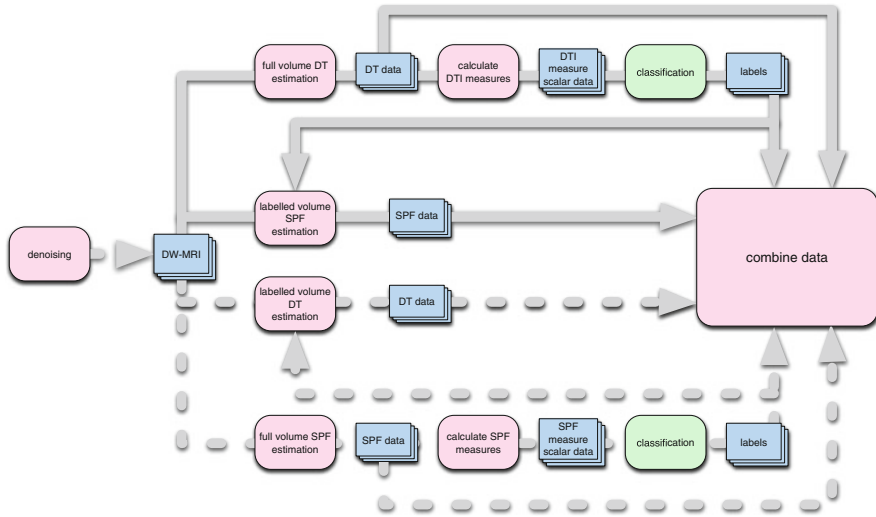


**Fig. 1** Schematic diagram of the pipeline for DTI and HARDI combination. The *blue stacked rectangles* represent data volumes. The *pink round rectangles* represent data transformations. The main contribution of this chapter is focused in the classification part colored as *green*. The *arrows* capture the flow of the process, whereas *dashed arrows* depict optional scenarios

voxel) or merits its drawbacks? In crossing areas, it is certainly justified, but for a large part of the white matter, there is a significant number of single fiber voxels where high-order modeling might be redundant. Thus, it is important to be able to classify regions of single fiber (anisotropic-Gaussian) and crossing fibers (non-Gaussian) in white matter in a fast and reliable way. This can lead to reducing the modeling complexity in areas where it is not needed and enabling possibilities for data simplification. The advantages would be significant for further post-processing and visualization of the data, especially with respect to reducing computer memory requirements. This will undoubtedly make HARDI data easier to manipulate and interact with, making it more attractive for clinical applications.

One possibility for fast classification of the DW-MRI data is by identifying the type of anisotropy in each voxel by some of the anisotropy measures for DTI and HARDI. These measures are fast to calculate since they are scalar measures calculated on the eigenvalues of the diffusion tensor,  $\mathbf{D}$ , in the first case or the SH coefficients in the latter.

Classification of the data by these measures in three compartments will allow masking of the data in the isotropic areas where the gray matter and the ventricles belong, using simple diffusion tensor model in the anisotropic-Gaussian regions and applying more sophisticated high order modelings in the non-Gaussian regions in a fast manner. There are two ways in which we can look at this problem for data combination and thus, simplification (see Fig. 1).

In the first scenario, from the DW-MRI data (that can be additionally denoised) we can calculate the DT model and apply scalar anisotropy measures that label the data into three compartments. Afterwards, in the compartment labeled as

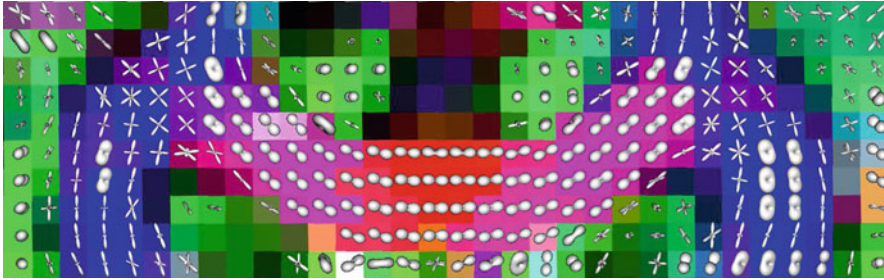


**Fig. 2** Example of hybrid visualization of CSD [6] and 2nd order ODFs

non-Gaussian, more complex HARDI modeling techniques that provide more accurate local intra-voxel information can be applied. This allows reducing of the postprocessing time in comparison with full data volume modeled by HARDI techniques and better memory management: one value in the area labeled as isotropic, a diffusion tensor for the anisotropic Gaussian areas and the rest modeled with high-order SPFs. However, this would require reliable classification by the DTI measures especially with respect to small number of false positives in the labeling, since this would underestimate the data.

In the second scenario, we model the data by a HARDI modeling technique (preferably by linear models like ADC or Q-Ball that are relatively fast to calculate) and then apply HARDI anisotropy measures. These measures also label the data into three compartments, and similarly the data can be modeled by DT or HARDI SPFs. In this scenario, to get better angular resolution, we can additionally choose to apply a non-linear (more time demanding) technique as constrained spherical deconvolution (CSD) [6, 7] for the non-Gaussian regions. Presenting the data by combining both of the data representation models would benefit in faster visualizations with better context especially since the data in the anisotropic Gaussian regions would be significantly simplified.

As an example, in Fig. 2 we show a hybrid visualization of the simplified data (labeling provided by generalized anisotropy (*GA*) classification) from an in-vivo dataset represented by 8th order CSD [6] in the non-Gaussian classified regions, and 2nd order ODFs in the anisotropic-Gaussian regions. The combining process follows the second scenario described previously. The difference in running time from the most naive implementation of CSD, is as follows. Computing CSD of order 8 for the whole brain in white matter mask: 540 min (36,601 voxels). Computing CSD of order 8 in labeled crossing : 120 min (8,164 voxels). Computing 2nd order ODFs in labeled linear : 19 s.<sup>1</sup> With hybrid data modeling, there is a gain of almost

<sup>1</sup>These times were calculated on a 1.66 GHz processor dual core Intel machine with 2 GB of RAM. CSD is a non-linear method that takes several iteration to perform the constrained regularization, which goes back and forth between at least 300 points on the sphere and the order 8 SH representation. This can be greedy and in our implementation takes approximately 0.5–1 s per

factor 5 in time for computation compared to modeling full brain data with the same high order model. Also interaction in the visualization pipeline becomes possible, even for a full brain slice.

In this work we examine and compare the classification power of different DTI and HARDI anisotropy measures. Additionally, we try to answer whether there is a significant gain from the measures calculated from the more complex HARDI models. We use pattern recognition schemes for investigating the classification potentials of these measures on a ground truth *ex-vivo* phantom under different b-values. Furthermore we show some qualitative real data results that corroborate some of the conclusions from the phantom data. To improve the quality of the real data scanned under clinically acceptable schemes, we use a denoising scheme [8] that recommends improvement of the coherence of the classified regions. We thus come to several conclusions suggesting that HARDI processing and data interaction are possible in a clinical setting.

## 2 Related Work

The work of Alexander et al. [3], is among the first that classifies the data in three compartments: isotropic, anisotropic-Gaussian, and non-Gaussian. This work uses ANOVA F-test based on the SH representation of the apparent diffusion coefficient (ADC) profile for several truncation orders  $l_{max}$ . Comparison of the measured ADC with the estimated one is required in each step, and therefore this process is slow and memory consuming. Furthermore it is necessary to calculate a critical value for the F-test to achieve stopping criteria, and this threshold is difficult to find given that the whole process is not interactive. Behrens et al. [9] use automatic relevance determination integrated in a Bayesian modeling framework to simplify the problem of tracking in a multi-orientation field. Hosey et al. [10] use an extension of a Markov chain method that infers the probability density function of up to two intra-voxel fiber orientations. However, both of the mentioned techniques are computationally intensive to implement. This is mainly due to the Bayesian estimation of the parameters making these methods iterative, with lack of simple user interaction. Interactive data classification can be of great importance for simplification of the HARDI data, especially in the case of clinical applications. It is also valuable for immediate identification of uncertainty regions in the DTI-based fiber tracking that has already been used widely. The speed in accurate identification of anisotropic-Gaussian and non-Gaussian regions in the data can accelerate the whole postprocessing pipeline for the complex HARDI data. Wide range of anisotropy measures has been proposed in literature [2, 4, 11–15]. Several authors [3, 12, 13] have attempted to use some of these measures to classify non-Gaussian profiles, but all these attempts have been made on the apparent diffusion

---

voxel. This time can obviously be improved by parallelizing the code and changing the parameters of CSD regularization (less iteration and faster stopping criteria).

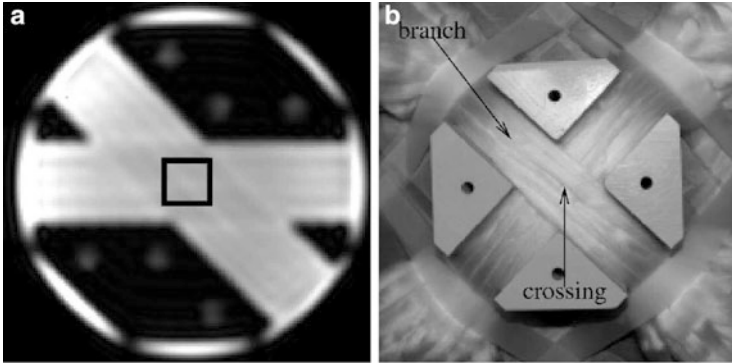


**Fig. 3** (a) Fast spin-echo map and a region of interest for the crossing voxels of the  $45^\circ$  *ex-vivo* phantom and (b) Picture of the  $90^\circ$  *ex-vivo* phantom

coefficient (ADC) profiles and without convincing real data results. In our previous work [16], we applied these HARDI anisotropy measures not only to ADC profiles but to different spherical probability functions like Q-Ball and the DOT. In this chapter, however, we extend the previous ad-hoc analysis by thorough examination of the classification power of the measures by ROC curves, histograms and scatter plots. We additionally extend the analysis to DTI anisotropy measures and compare their classification power with the measures derived from HARDI data.

### 3 Diffusion Data Acquisition

The details of the *ex-vivo* phantom data and in-vivo human data used in this study are explained below.

***Ex-vivo phantom:*** To test our classification measures, we use two *ex-vivo* phantoms with fibre bundles crossing at  $45^\circ$  and  $90^\circ$  [17] (Fig. 3). These datasets serve as ground truth, where the number of crossing voxels is known. The phantom data was acquired on a 1.5T Signa MR system (GE Healthcare), TE/TR = 130 ms/4.5 s, 12.0 s ( $45^\circ$  and  $90^\circ$  phantom, respectively), BW = 200 KHz. We analyze the data acquired at two b-values of  $b = 2,000$  and  $b = 8,000$  s/mm<sup>2</sup>, along 200 uniform directions.

***Human:*** Diffusion acquisitions were performed using a twice focused spin-echo echo-planar imaging sequence on a Siemens Allegra 3T scanner, with FOV  $208 \times 208$  mm, isotropic voxels of 2 mm. Ten horizontal slices were positioned through the body of the *corpus callosum* and *centrum semiovale*. Uniform gradient direction schemes with 49 and 121 directions were generated with the electrostatic repulsion algorithm [18] and the diffusion-weighted volumes were interleaved with  $b_0$  volumes every 12th scanned gradient direction. Datasets were acquired at b-values of 1,000, 1,500, 2,000, 3,000, 4,000 s/mm<sup>2</sup> and in the same session, two anatomical data sets (192 slices, isotropic 1 mm voxels)

were acquired using the ADNI sequence for registration. Finally, before HARDI reconstruction of the ADC, Q-Ball and DOT, we applied a denoising pre-processing step [8], available online,<sup>2</sup> to correct for the Rician noise bias in the datasets.

## 4 Methods

### 4.1 HARDI Measures

We implemented several HARDI anisotropy measures from the literature: generalized anisotropy (GA) [14], generalized fractional anisotropy (GFA) [4], the cumulative residual entropy (CRE) [11, 12], as well as fractional multifiber index (FMI) [2], and  $R_0$ ,  $R_2$ ,  $R_i$  [13] (see Table 1). Most of the measures are calculated directly from the SH coefficients of the corresponding spherical probability functions and therefore are extremely fast to calculate.

These measures were applied on the ADC profiles [2, 3], analytical Q-ball [19] and the DOT [5]. Since the DOT was originally proposed in complex SH basis, we adapted it to real SH, and solve the spherical harmonic transform in the parametric DOT by least-square fit. This way we obtain a probability density function (PDF) represented in real spherical harmonic coefficients, and all the anisotropy measures can be applied to it. The DOT generally produces much sharper glyph profiles for high radius  $Rad_0$ , at the cost of more noisy profiles with spurious peaks. Finding the *best*  $Rad_0$  in real data is difficult and often done by visual observation [5]. Hence, to avoid this  $Rad_0$  selection problem and inspired by definitions of the ODF from Q-ball imaging [4] and the marginal ODF (mODF) from diffusion spectrum imaging (DSI) [20], we propose similar ODFs computed from the DOT as:

$$\begin{aligned}\psi_{\text{DOT-ODF}}(\theta, \phi) &= \int_0^{Rad_{0max}} P(r, \theta, \phi) dr, \\ \psi_{\text{DOT-mODF}}(\theta, \phi) &= \int_0^{Rad_{0max}} P(r, \theta, \phi) r^2 dr,\end{aligned}\tag{2}$$

where  $P(r, \theta, \phi)$  is the PDF computed from DOT [5], and  $Rad_0$  is set to a conservatively high value.

As a discrete binary measure for the classification, we propose the number of maxima (NM). NM uses the number of local maxima of the min-max normalized SPFs profiles, where the discrete spherical function surpasses a certain threshold (here, we use 0.6) from points on a fine discrete mesh (5th order of tessellation of icosahedron), using a finite difference search on the mesh points. Moreover, for

---

<sup>2</sup><http://www.iris.fr/visages/benchmarks/>

**Table 1** Scalar measures for HARDI.  $a_{lm}$  are spherical harmonics coefficients of order  $l$  and phase  $m$ 

Name	Abbrev.	equation
Generalized anisotropy [14]	$GA$	$GA = 1 - \frac{1}{1 + (250 \text{ V})e^{(V)}}$ <p>where <math>e(V) = 1 + \frac{1}{1 + 5,000 \text{ V}}</math>,</p> $V = \frac{1}{9a_{00}^2} \sum_{l=2}^{l_{max}} \sum_{m=-l}^l  a_{lm} $
Generalized fractional anisotropy [4]	$GFA$	$GFA = \sqrt{1 - \frac{a_{00}^2}{\sum_{l=0}^{l_{max}} \sum_{m=-l}^l  a_{lm} }}$
Cumulative residual entropy [11, 12]	$CRE$	$CRE = - \sum_{i=2}^M P(\psi_n > \lambda_i) \log P(\psi_n > \lambda_i) \Delta \lambda_i,$ <p>where <math>\lambda_1 &lt; \dots &lt; \lambda_M</math>, <math>\psi_n = \psi_{norm}(\theta, \phi)</math></p>
Fractional multi-fiber index [2]	$FMI$	$FMI = \frac{\sum_{l=4}^{l_{max}} \sum_{m=-l}^l  a_{lm} ^2}{\sum_{l=2}^{l_{max}} \sum_{m=-l}^l  a_{lm} ^2}$
Isotropic ratio [13]	$R_0$	$R_0 = \frac{ a_{00} }{\sum_{l=0}^{l_{max}} \sum_{m=-l}^l  a_{lm} }$
Linear ratio [13]	$R_2$	$R_2 = \frac{\sum_{l=2}^{l_{max}} \sum_{m=-l}^l  a_{lm} }{\sum_{l=0}^{l_{max}} \sum_{m=-l}^l  a_{lm} }$
Multi-fiber ratio [13]	$R_i$	$R_i = \frac{\sum_{l=4}^{l_{max}} \sum_{m=-l}^l  a_{lm} }{\sum_{l=0}^{l_{max}} \sum_{m=-l}^l  a_{lm} }$

better visual perception, in our figures we generate min-max normalized RGB color coded glyphs, although one must keep in mind that this normalization enhances angular contrast of glyphs in the white matter but also deforms isotropic glyphs considerably.

**Table 2** Scalar measures for DTI.  $\lambda_1 > \lambda_2 > \lambda_3$  are the corresponding eigenvalues of the diffusion tensor  $\mathbf{D}$ 

Name	Abbrev. equation
Mean diffusivity [22]	$MD = \text{tr}(\mathbf{D})/3 = (\lambda_1 + \lambda_2 + \lambda_3)/3$
Fractional anisotropy [22]	$FA = \frac{\sqrt{(\lambda_1 - \lambda_2)^2 + (\lambda_2 - \lambda_3)^2 + (\lambda_1 - \lambda_3)^2}}{\sqrt{2(\lambda_1^2 + \lambda_2^2 + \lambda_3^2)}}$
Relative anisotropy [22]	$RA = \frac{\sqrt{(\lambda_1 - \lambda_2)^2 + (\lambda_2 - \lambda_3)^2 + (\lambda_1 - \lambda_3)^2}}{\sqrt{2(\lambda_1 + \lambda_2 + \lambda_3)}}$
Linear anisotropy [21]	$C_l = (\lambda_1 - \lambda_2)/(\lambda_1 + \lambda_2 + \lambda_3)$
Planar anisotropy [21]	$C_p = 2(\lambda_2 - \lambda_3)/(\lambda_1 + \lambda_2 + \lambda_3)$
Isotropy [21]	$C_s = 3\lambda_3/(\lambda_1 + \lambda_2 + \lambda_3)$

## 4.2 DTI Measures

We implemented DTI anisotropy measures: linear anisotropy  $C_l$ , planar anisotropy  $C_p$  and isotropy  $C_s$  [21] as well as the well-known fractional anisotropy ( $FA$ ) and mean diffusivity ( $MD$ ) [22] (see Table 2).

These measures were applied on the diffusion tensors estimated from the same DW-MRI data as used for the HARDI modeling.

## 4.3 Analysis of Measures

To quantify the classification power of the DTI and HARDI measures, we use the statistical test of receiver operation characteristic (ROC) curves [23] for the hardware phantom data. The ROC curves describe the classification power of each of the measures for separation of the data into three distinct compartments: isotropic, non-Gaussian and anisotropic-Gaussian by using two thresholds. We apply this analysis only to the phantom data, since only there we know the ground truth for crossing voxels. Furthermore, we explore the distributions of the values from each measure in different phantom data configurations by histograms. At the end we suggest some interesting combinations of different measures for improving the classification power of the individual measures. In addition, we discuss the differences between DTI and HARDI measures. We describe each of these analysis in details below.

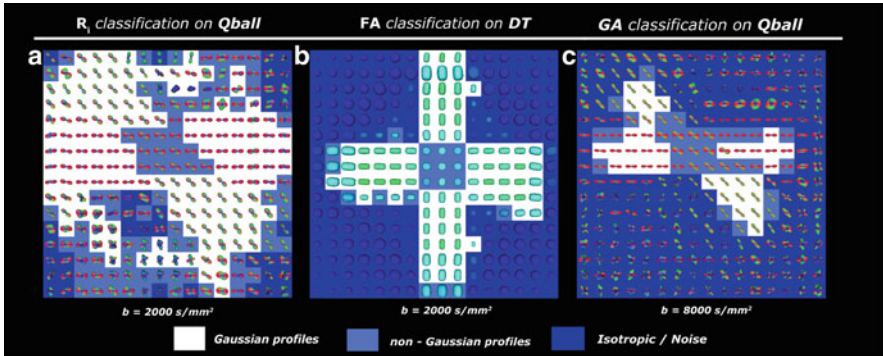


Fig. 4 Classification results from the phantom data

### 4.3.1 Different Phantom Configurations

Before explaining the data analysis we would like to review the *ex-vivo* phantom data and its configurations. We will derive our conclusions based on three different phantom crossing datasets varying either in configuration or b-value (see Fig. 4). We have the  $45^\circ$  of crossing phantom data, with exactly 12 voxels of ground truth crossings. The rest of the  $16 \times 16 = 256$  voxels belong to single fiber voxels (estimated to 64 voxels) and isotropic voxels considerably deformed by the MRI noise. The  $45^\circ$  angle of crossing is a challenging angle where most of the HARDI techniques fail to recover multiple fiber populations, especially at low b-values. Therefore we investigate this configuration under two different b-values of 2,000 and 8,000  $\text{s/mm}^2$ . In addition we analyze the phantom data of  $90^\circ$  only at b-value of 2,000  $\text{s/mm}^2$  (b-value of 8,000  $\text{s/mm}^2$  is not interesting to analyze for this angular configuration). Here, we have exactly nine voxels of ground truth crossings and the rest belong to single fiber population and noise. There are a few points that we need to keep in mind. Due to partial volume effect, some of the linear voxels might exhibit non-Gaussian diffusion properties. Since this is to be expected in real data as well, we simply need to keep it in mind when analyzing the data. Due to the high SNR value of the *ex-vivo* phantom data, we do not need a denoising phase.

### 4.3.2 ROC and Histogram Analysis of the Phantom Data

For the DTI and HARDI anisotropy measures we can quantitatively describe their classification power using binary classification statistical test. First, the measures must be thresholded to obtain the classification, and this process is sensitive. Two thresholds are needed to separate the interval of anisotropy values into three distinct compartments: isotropic, non-Gaussian and anisotropic-Gaussian. Afterwards we can calculate the ROC curves that graphically represent the relationship between

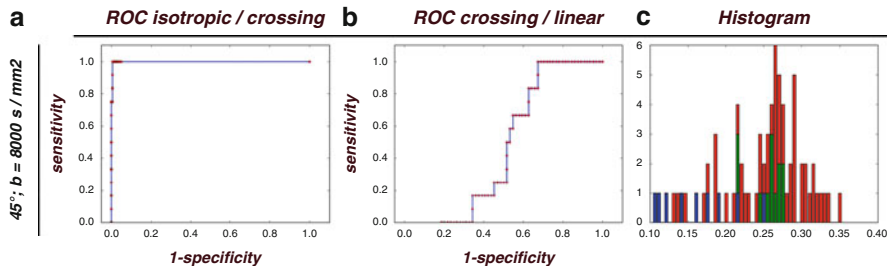


**Fig. 5** ROC curves for isotropic/crossing and crossing/linear scenario and histogram for FA applied to the 45° *ex-vivo* phantom data at b-value of 8,000 s/mm<sup>2</sup>. The color coding of the histogram: *blue*—isotropic, *green*—crossings, *red*—linear voxels

specificity and sensitivity of the voxels classified as: isotropic (from the noise), crossing (non-Gaussian) and linear (anisotropic-Gaussian) [23]. The sensitivity measures the proportion of actual positives which are correctly identified as such, and the specificity measures the proportion of negatives which are correctly identified.

$$sensitivity = \frac{\text{number of True Positives}}{\text{number of True Positives} + \text{number of False Negatives}} \tag{3}$$

$$specificity = \frac{\text{number of True Negatives}}{\text{number of True Negatives} + \text{number of False Positives}}$$

Since separation into three distinct compartments is desirable, we need to calculate two ROC curves per measure, one of which represents the classification power between isotropic and non-Gaussian profiles (Fig. 5a), and the other between non-Gaussian and anisotropic Gaussian (Fig. 5b). Calculating two ROC curves is possible due to the distribution of the anisotropy as low in the isotropic parts, medium in the non-Gaussian regions and high for anisotropic Gaussian. To quantify the accuracy of the measures we calculate and report the area under the ROC curves (see appendix). The larger the area under the curve, the better the separation of the profiles by the examined measure.

For illustrating the distribution of anisotropy values, we use histograms (Fig. 5c). However, as expected many DTI measures do not have this smooth transition, whereas most of the HARDI measures exhibit more desirable properties.

### 4.3.3 Scatter Plot Analysis for Combination of Measures

To investigate the possibilities of combining and thus increasing the classification power of the measures we do some preliminary experiments with scatter plots, where we combine different DTI and HARDI measures together and look at the distribution of the combined measure values (see Fig. 8).

## 4.4 Real Data Analysis

As we do not know the ground truth in real data, we cannot perform quantitative analysis. Therefore we limit our analysis to qualitative observations on the results from the classification of the data done by the same measures that were applied to the phantom data. Since the SNR of our clinically obtained DW-MRI data is very low (especially at high b-values), experiments were done by comparing the results with pre-denoised data.

### 4.4.1 Denoising of the Real Data

We use a non-local mean filter with Rician noise correction to denoise the DW data before HARDI reconstruction. This method was shown [8] to have the desired effect of correcting for the noise bias without blurring-out figure crossing information. Hence, it improves scalar measures extracted from DTI and HARDI and does not reduce the angular profiles of HARDI glyphs. The computation time of this filter depends on spatial resolution and the number of maxima. For example, on our real dataset of  $104 \times 104 \times 10 \times 121$ , the denoising takes 16 min when computed over four processors 3 GHz and 8 GB RAM.

## 5 Results

In this section, we present the quantitative analysis of the *ex-vivo* phantoms and qualitative results from the real data.

### 5.1 Phantom Results

The  $45^\circ$  is a challenging angle where most of the HARDI techniques struggle to detect multiple maxima, especially at low b-values. We will first analyze the results from the maxima detection. As pointed out in the work of Prčkovska et al. [24], DOT has the potential of recovering small angles regardless of the b-value, which we show in the table of Fig. 6. Only the DOT (and its derivations) manages to recover two fiber populations in the crossing regions at low combination of crossing angle and b-value (in this case  $45^\circ$  and  $2,000 \text{ s/mm}^2$ ). In the table we report the success at recovering two maxima in the crossing voxels by all of the examined SPFs for SH orders 4, 6 and 8. We additionally report the first  $Rad_0$  for the DOT and its derivations in which the success is greater than 50%. Even more interesting, we observe that the derivations of the DOT discussed in Sect. 4, with its ODFs (DOT-

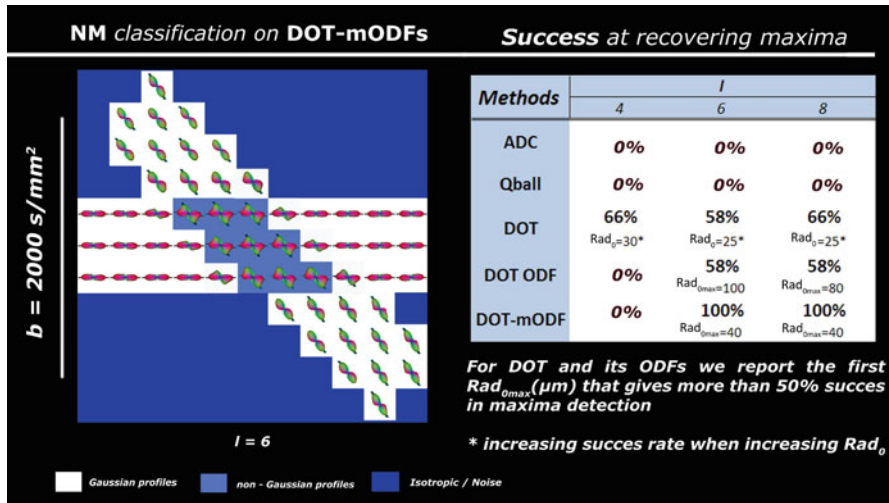
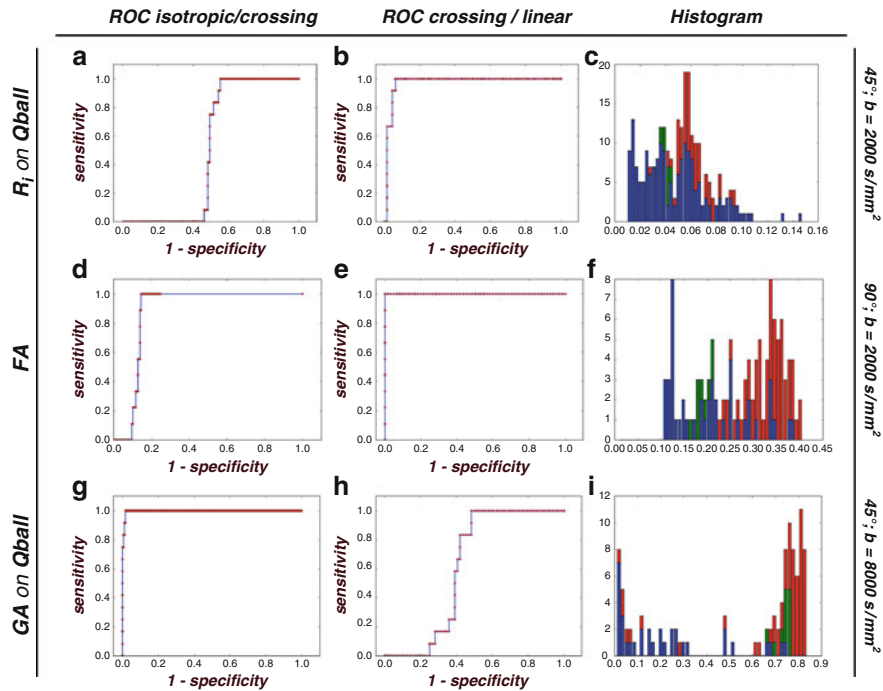


Fig. 6 Classification results from the 45° phantom data. The noise voxels were masked out by FA, since NM classification gives multiple maxima in these areas

ODF and DOT-mODF) manifest similar behavior to the DOT itself, which show a better angular resolution than Q-Ball and suggest a better choice of reconstruction algorithm for fiber tracking purpose. The results from the NM classification on the 90° phantom are omitted, due to the 100 % success in the classification of the non-Gaussian voxels demonstrated in all reconstruction methods. Increasing the b-value to 8,000 s/mm<sup>2</sup> improves the angular resolution of Q-Ball as expected, and crossings are starting to be observed in the 45° dataset. We presented the classification results from the real data to an anatomist who evaluated the accuracy of the classification, and suggested preferences over some of the results. In the following paragraphs, as we discuss the real data results we include the feedback from the anatomist.

For the DTI and HARDI anisotropy measures, we can quantitatively describe the classification power of the 45° and 90° phantoms by examining the shape of the corresponding ROC curves, and calculating the area under the ROC curves. Additionally we observe the distribution of the measure values in the histograms as described in Sect. 4.3.2. In the appendix, the area under all of the examined DTI and HARDI ROC curves is reported. From the observation of the ROC curves and the values of the area under the ROC curves, we draw several conclusions. Increasing the order of SH representation does not significantly improve the classification power of the measures. Therefore, for simplicity, in our phantom data results we report only an SH order of 4. For the DOT derivations (DOT-mODF and DOT ODF) the results become worse at high SH order, due to the very high and densely distributed anisotropy values. The DOT in every configuration and SH order gives



**Fig. 7** ROC and histogram examples from the phantom data. The coloring in the histograms indicates: *blue*—isotropic, *green*—crossings, *red*—linear

bad results due to the reasons mentioned above, even though it produces sharper angular profiles. Also the measures applied to DOT derivations in general produce worse results than those applied to the rest of the HARDI models. This can be observed in the appendix Fig. A.1a colored with red stating bad classifier. Most of the measures (DTI and HARDI), are significantly better in separating the data between isotropic and crossing voxels (see Fig. 7d, g; Fig. A.1a, b). The DTI measures even outperform the HARDI measures in many cases (see Fig. 7a, d); however, note that the presented results are for different angular configurations). For the separation of the crossing and linear areas, on the other hand, the situation is more complex. In general, many HARDI measures like *CRE*, *GA*, *GFA* and *R2* on ADC and Q-Balls have medium classification power and are comparable to the DTI measures like *C<sub>l</sub>*, *FA* and *MD*. Notably bad in many scenarios appear to be *C<sub>p</sub>*. A measure that stands out for good classification, especially of the challenging 45° angle between crossing and linear combinations, is *R<sub>i</sub>* applied on Q-Balls. This is to be expected, given the definition of the measure (see Fig. 7b).

From our *ex-vivo* phantom study we can conclude that the classification power between anisotropic Gaussian and non-Gaussian areas of the HARDI measures

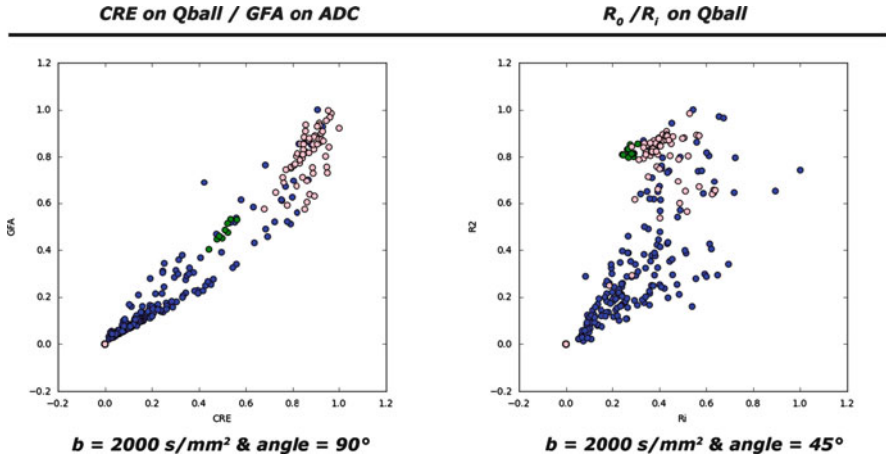


**Fig. 8** Scatter plots from combination of different measures. *Blue* color stands for isotropic voxels, *green* crossing voxels and *red* single fiber voxels

in general is slightly better than that of the DTI measures. This difference is more prominent at smaller angles of crossings. For distinguishing isotropic from non-Gaussian regions, the DTI measures outperform HARDI measures. The distribution of the anisotropy values from low to high following the isotropic/non-Gaussian/anisotropic-Gaussian pattern, is more noticeable in the HARDI measures like *GA*, *GFA* and *CRE* (e.g., Fig. 7f, i).  $R_i$  on Q-Balls is a good classifier between non-Gaussian and anisotropic-Gaussian regions.

There is potential in combining measures to increase the separation between classes. Some measures show a better separation between isotropic and non-Gaussian, and others between non-Gaussian and anisotropic Gaussian. Furthermore, some measures perform better when applied to different SPFs. Preliminary results suggest that combination of *CRE* and *GFA* on Fig. 8 left and  $R_i$  and  $R_2$  on Fig. 8 right can improve the classification power of the measures.

### 5.1.1 Human Data Results

The *centrum semiovale* was used to illustrate the qualitative analysis of the classification results. It is an interesting region for analysis, since fibers of the *corpus callosum* (CC), *corticospinal tract* (CST), and *superior longitudinal fasciculus* (SLF) form different two-fiber and three-fiber crossing configurations in that area. The region-of-interest (ROI) was defined on a coronal slice (see Fig. 9a). It is important to mention that all the real data results are from similar regions, since they are different DW-MRI scans from the same subject, and have not been registered. We presented the classification results to an anatomist who evaluated the accuracy

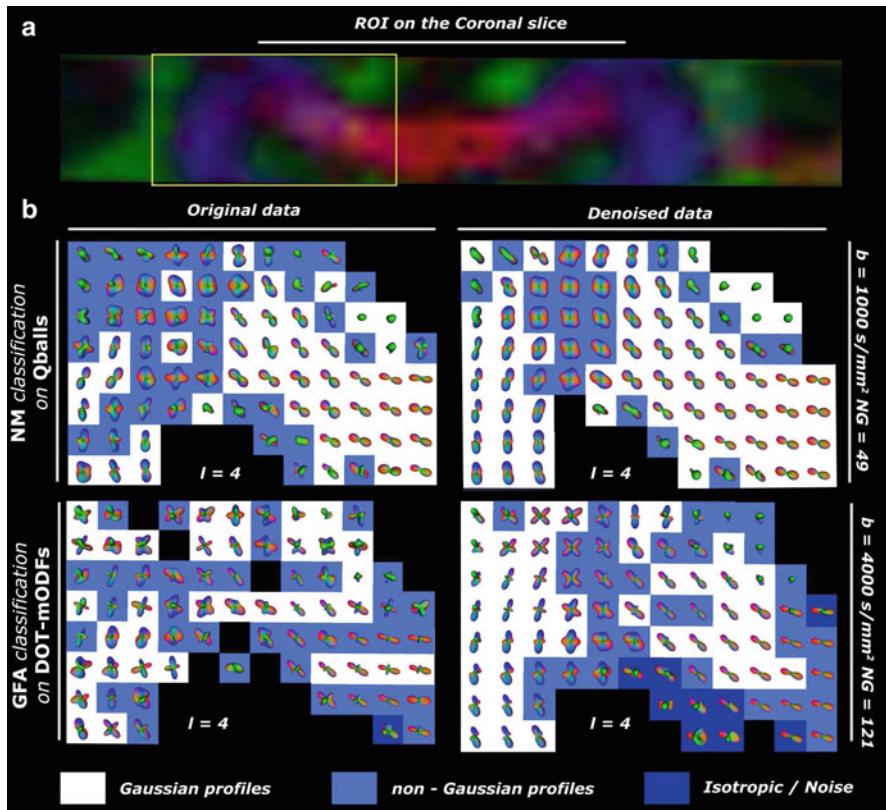


**Fig. 9** The effect of denoising demonstrated on original versus denoised data in different acquisition schemes

of the classification, and suggested preferences over some of the results. In the following paragraphs, as we discuss the real data results we include the feedback from the anatomist. We applied the same classification measures as for the phantom study on the original and denoised data from our datasets. Denoising significantly improves the glyph profiles and the coherence of the non-Gaussian regions, as seen in Fig. 9. We also observe a decrease in the irregularities in the crossing profiles. Our results suggest that even at low  $b$ -value, low NG and low estimation SH order, there is success in recovering crossing diffusion patterns and identifying linear regions (see Fig. 10). The feedback from the anatomist followed the same rule. In general most of the classification done under  $b$ -value of  $1,000 \text{ s/mm}^2$  and low sample of the gradients were found to be the best. For instance in Fig. 10 the classification from CRE applied to DOT-mODF at  $b = 1,000 \text{ s/mm}^2$  and  $NG = 49$  was found to be the best due to the well spread crossing region.

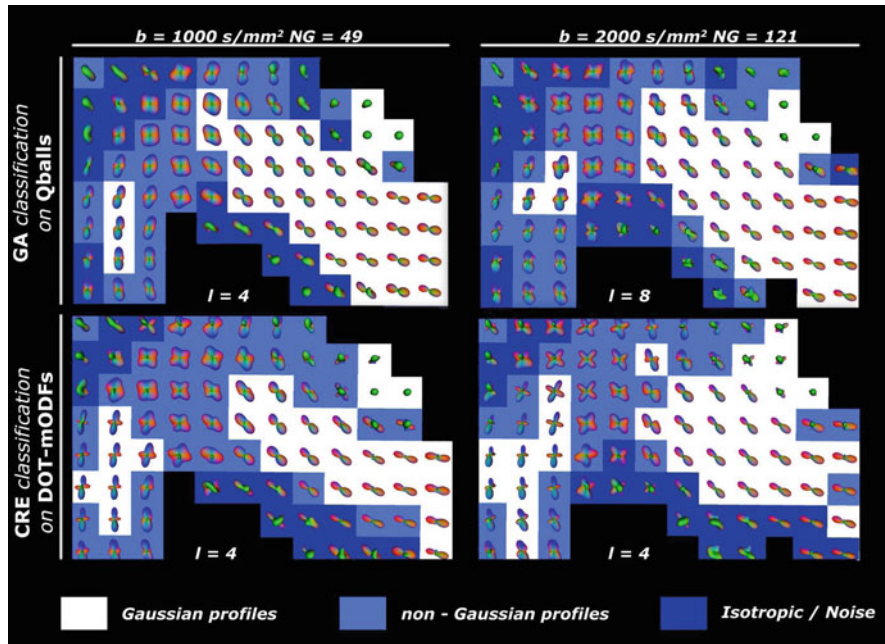


**Fig. 10** Some examples from different classifications applied to in-vivo human data from the region of *centrum semiovale*

In contrast, going to very high b-values (i.e.  $\geq 3,000$  s/mm<sup>2</sup>) and modeling the data with high SH order ( $\geq 6$ ) results in polluted glyphs regardless of whether denoising is performed. Comparing the results of the classification from different measures, we observe that increasing the b-value sharpens the HARDI profiles and benefits only for maxima extraction purposes. However, there is no significant gain in classification of non-Gaussian profiles, as observed in the phantom study. This is seen in Fig. 10, where we see sharper glyphs for DOT-mODF but similar classification power regardless of the measure or acquisition scheme. We also note that increasing the model order ( $l > 4$ ) does not increase the classification power, which coincides with the conclusions from our phantom study. This leads to the conclusion that 49 directions is sufficient for recovering most of the crossings and non-Gaussian voxels, which means that the acquisition time can be significantly reduced (compared to a 121 NG acquisition).

Figure 11 demonstrates a comparison between  $FA$  and  $R_i$ . We observe that  $FA$  exhibits similar classification properties to the ones observed in 90° phantom, thus giving a nice contrast in the *centrum semiovale*.  $R_i$  on the other hand, has a bigger problem separating isotropic areas from non-Gaussian ones, which reference the poor performance in the isotropic/crossing ROC curve (Fig. 7a).

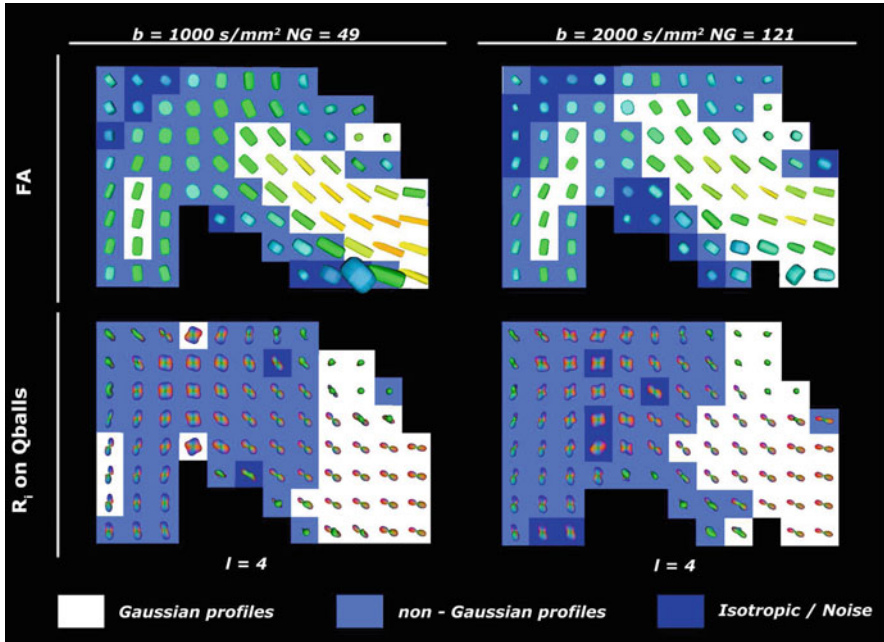


Fig. 11 Comparison DTI versus HARDI classification

The anatomist similarly found the classification from  $FA$  at  $b = 1,000 \text{ s/mm}^2$  and  $NG = 49$  to outperform the one from the higher  $b$ -value and denser gradient sampling. The classifications from  $R_i$  were found to have over-classified crossing area.

## 6 Discussion and Conclusions

Finding the correct threshold for classification in real data is important for accurate classification, and often depends on the  $b$ -value from the acquisition protocol and the angular configuration. In our study, the thresholds found in the  $90^\circ$  phantom configuration were very similar to the thresholds used to classify the real data at the same  $b$ -value. The thresholding process for the in-vivo data can be significantly improved by a semi-automatic algorithm for detection of the thresholds. The user can additionally give feedback by identifying regions with positive and negative examples.

There are a few important messages from this work. Denoising as a pre-processing step improves the coherence of the classification areas and enhances the

HARDI profiles, as reported by Descoteaux et al. [8]. ADC and Q-Ball demonstrate significant classification information, even though they sometimes lack sufficient angular resolution for small crossing-angle discrimination. The sharper and slightly more noisy profiles produced by DOT and its derivation (and we believe this would be the case for SD techniques [7] as well) find more accurate numbers of maxima and are better suited for fiber tracking applications. Increasing the acquisition parameters ( $b$ -value  $> 2,000$  s/mm<sup>2</sup> and NG  $> 80$ ) as well as the model order do not significantly improve the classification power. In contrary, high  $b$ -value acquisitions produce low SNR datasets that are worse for classification, and result in polluted HARDI profiles. This corroborates the observations from the anatomist, who found the classifications applied on data with  $b = 1,000$  s/mm<sup>2</sup> and NG = 49 to be the best. It is even doubtful if, in practice, these higher  $b$ -value datasets improve fiber tracking. Further studies would be needed to be able to estimate the exact optimal acquisition parameters for classification. For example, it would be interesting to acquire *ex-vivo* ground truth crossing phantoms with a higher variety of acquisition parameters. The results of the study presented in this chapter indicate that the optimal acquisition will be possible in a clinical environment, since relatively low acquisition time will be needed for the preferred acquisition parameter setting. DTI anisotropy measures are comparable with the HARDI measures like  $GA$ ,  $GFA$  and  $CRE$  and in classifying isotropic from crossing regions often outperform.

In this work, we investigated a broad range of different DTI and HARDI anisotropy measures proposed in the literature and applied them as classification criteria for discriminating different fiber configurations within the white matter. All the measures were applied on the HARDI reconstructions and all, except for  $CRE$  and  $NM$ , are measures directly implemented on SH representation of the model or DT that can be calculated and thresholded in real time. Some of the measures such as  $GA$ ,  $GFA$  and  $CRE$  applied on Q-balls and ADC behave in a similar fashion and are relatively good classification criteria. However, their power is comparable to DTI measures such as  $FA$  and  $MD$ .  $R_i$  exhibits strong classification power for separating crossings from linear areas even at low angle. However, due to the poor isotropic/crossing performance, it is recommended combining it with other measures. The  $NM$  measure belongs to a different category of measures because it does not need a thresholding process for classification. However, it is dependent on the HARDI profiles and can produce many false positives in the presence of noise.

A strong message that comes out of this work, is that the measures can be applied on different SPFs and still have the same classification power (especially in the case of ADC and Q-Ball). This means that the users can use any existing HARDI modeling technique and apply classification measures to distinguish between anisotropic-Gaussian and non-Gaussian profiles. If the non-Gaussian voxels are correctly classified in a first step, one can ignore all the other single fiber voxels and properly focus on the modeling and more accurate reconstruction of these voxels. Hence, as a second step, one can use a complex modeling approach, such as CSD and PAS-MRI [25] that take long computation time. In clinical setting, the simplification of the data into anisotropic-Gaussian and non-Gaussian areas can

be useful and presents a new contrast as such, even though complex structures are oversimplified as non-Gaussian. It can lead to new ways to study the white matter, especially by enabling the possibility for interactive visualization and inspection of the data.

Future work will address combination of different measures for better reliability of the classified regions. Comparison of our simple and fast classification with some of the existing classification schemes (as in the work of Schnell et al. [26]) is addressed as future work. These methods use support vector machines or learning approach such as boosting on the entire set of measures to statistically determine the discriminative strength of each feature and therefore cannot be calculated at interactive speed. Thus, the comparison should be done for validation purposes of the methods only.

In this chapter, we are not dealing with the behavior of the classification in partial volume effect regions. If there is partial volume effect between different classes, it is expected that the selected model will correspond to the one that can represent the most complex configuration. For example, in the case of partial volume effect between isotropic and anisotropic-Gaussian, the voxel will be classified as anisotropic-Gaussian. Further studies would be necessary to determine the validity of this assumption.

Nonetheless, in this work we have shown that possible classification of anisotropic-Gaussian and non-Gaussian profiles can be done with some of the existing measures including scalar indices calculated from DTI data. For the DTI indices, however, we need to be careful as the distribution of the anisotropy values does not always follow the isotropic/non-Gaussian/anisotropic-Gaussian pattern. The data can therefore be simplified into linear, crossing and isotropic voxels. This means that more sophisticated hybrid methods, which are more time consuming can be applied only in the non-Gaussian areas, whereas in the anisotropic-Gaussian the profiles can be modeled with a simple 2nd order ODFs (see Fig. 2) and the isotropic profiles masked out. This gives considerable potential for the employment of the HARDI techniques in a clinical setting due to the moderate post-processing time. Another application of the classification information can be in visualizing uncertainties in fiber tracking algorithms by, for example, attributing transparency to the unreliable fiber tracts.

**Acknowledgements** We thank Alard Roebroek from Maastricht Brain Imaging Center, Department of Cognitive Neuroscience, Faculty of Psychology, Maastricht University, The Netherlands and Pim Pullens from Brain Innovation B.V., Maastricht, The Netherlands for providing us with in-vivo datasets. This study was financially supported by the VENI program of the Netherlands Organization for Scientific Research NWO (Anna Vilanova) and by the Netherlands Organization for Scientific Research (NWO), project number 643.100.503 MFMV (Vesna Prčkovska).

## Appendix

**a**

Measure	Profile	Cross/Linear			Average	Noise/Cross			Average
		$b=2000s/mm^2$		$b=8000s/mm^2$		$b=2000s/mm^2$		$b=8000s/mm^2$	
		45°	90°	45°		45°	90°	45°	
CRE	adc	0,671	1,000	0,409	0,693	0,938	0,864	0,999	0,934
	dot	0,310	0,256	0,346	0,304	0,656	0,614	0,413	0,561
	dotodf	0,408	0,776	0,376	0,520	0,908	0,127	0,979	0,671
	mdotodf	0,411	0,850	0,421	0,561	0,907	0,736	0,981	0,875
	qball	0,755	1,000	0,622	0,793	0,895	0,856	0,997	0,916
FMI	adc	0,551	0,107	0,660	0,439	0,091	0,070	0,008	0,056
	dot	0,785	0,761	0,754	0,767	0,317	0,228	0,748	0,431
	dotodf	0,633	0,663	0,608	0,635	0,132	0,157	0,485	0,258
	mdotodf	0,589	0,333	0,471	0,464	0,091	0,514	0,249	0,284
	qball	0,678	0,720	0,691	0,697	0,044	0,041	0,037	0,041
GA	adc	0,680	1,000	0,530	0,737	0,934	0,875	0,998	0,936
	dot	0,000	0,000	0,000	0,000	0,000	0,000	0,000	0,000
	dotodf	0,394	0,496	0,365	0,418	0,915	0,702	0,986	0,868
	mdotodf	0,902	0,618	0,994	0,838	0,025	0,445	0,000	0,157
	qball	0,749	1,000	0,611	0,786	0,898	0,873	0,997	0,923
GFA	adc	0,680	1,000	0,530	0,737	0,934	0,875	0,998	0,936
	dot	0,000	0,000	0,000	0,000	0,000	0,000	0,000	0,000
	dotodf	0,393	0,494	0,363	0,417	0,915	0,702	0,986	0,868
	mdotodf	0,902	0,617	0,995	0,838	0,025	0,444	0,000	0,157
	qball	0,749	1,000	0,611	0,786	0,898	0,873	0,997	0,923
R0	adc	0,475	0,000	0,605	0,360	0,074	0,187	0,001	0,087
	dot	0,801	0,778	0,824	0,801	0,318	0,228	0,756	0,434
	dotodf	0,602	0,524	0,633	0,586	0,089	0,234	0,017	0,113
	mdotodf	0,456	0,185	0,171	0,270	0,300	0,740	0,843	0,628
	qball	0,216	0,000	0,439	0,218	0,142	0,214	0,002	0,119
R2	adc	0,521	1,000	0,133	0,551	0,944	0,838	0,999	0,927
	dot	0,823	1,000	0,758	0,860	0,878	0,698	0,973	0,850
	dotodf	0,411	0,493	0,371	0,425	0,907	0,915	0,979	0,934
	mdotodf	0,405	0,826	0,368	0,533	0,911	0,044	0,982	0,646
	qball	0,570	1,000	0,152	0,574	0,940	0,828	0,999	0,923
Ri	adc	0,430	0,124	0,771	0,442	0,316	0,605	0,981	0,634
	dot	0,000	0,000	0,000	0,000	0,000	0,000	0,000	0,000
	dotodf	0,543	0,500	0,633	0,559	0,114	0,078	0,029	0,074
	mdotodf	0,598	0,204	0,632	0,478	0,089	0,952	0,017	0,353
	qball	0,973	1,000	0,760	0,911	0,501	0,529	0,980	0,670

**b**

Measure	Cross/Linear			Average	Noise/Cross			Average
	$b=2000s/mm^2$		$b=8000s/mm^2$		$b=2000s/mm^2$		$b=8000s/mm^2$	
	45°	90°	45°		45°	90°	45°	
Ca	0,482	0,672	0,496	0,550	0,220	0,208	0,049	0,159
Cl	0,724	1,000	0,521	0,748	0,910	0,772	0,998	0,894
Cp	0,038	0,000	0,039	0,026	0,944	1,000	0,999	0,981
FA	0,676	1,000	0,470	0,715	0,934	0,874	0,999	0,935
MD	0,846	0,878	0,595	0,773	0,840	0,859	0,992	0,897
RA	0,676	1,000	0,470	0,715	0,934	0,874	0,999	0,935

**Fig. A.1** Areas under the ROC curves for (a) HARDI and (b) DTI models. The higher the value the better the measure is for classification of the data. The color stand for *green*—good classifier; *red*—bad classifier

## References

1. Basser, P.J., Mattiello, J., LeBihan, D.: MR diffusion tensor spectroscopy and imaging. *Biophys. J.* **66**(1), 259–267 (1994)
2. Frank, L.R.: Characterization of anisotropy in high angular resolution diffusion-weighted mri. *Magn. Reson. Med.* **47**(6), 1083–99, (2002)

3. Alexander, D.C., Barker, G.J., Arridge, S.R.: Detection and modeling of non-gaussian apparent diffusion coefficient profiles in human brain data. *Magn. Reson. Med.* **48**(2), 331–40, (2002)
4. Tuch, D.: Q-ball imaging. *Magn. Reson. Med.* **52**, 1358–1372 (2004)
5. Özarslan, E., Shepherd, T.M., Vemuri, B.C., Blackband, S.J., Mareci, T.H.: Resolution of complex tissue microarchitecture using the diffusion orientation transform (DOT). *NeuroImage* **36**(3), 1086–1103 (2006)
6. Tournier, J.D., Calamante, F., Connelly, A.: Robust determination of the fibre orientation distribution in diffusion MRI: non-negativity constrained super-resolved spherical deconvolution. *NeuroImage* **35**(4), 1459–1472 (2007)
7. Jian, B., Vemuri, B.C.: A unified computational framework for deconvolution to reconstruct multiple fibers from Diffusion Weighted MRI. *IEEE Trans. Med. Imaging* **26**(11), 1464–1471 (2007)
8. Descoteaux, M., Wiest-Daesslé, N., Prima, S., Barillot, C., Deriche, R.: Impact of Rician Adapted Non-Local Means Filtering on HARDI. In: *MICCAI*, Berlin/New York, vol. 5242, pp. 122–130. Springer, Berlin (2008)
9. Behrens, T.E., Johansen-Berg, H., Jbabdi, S., Rushworth, M.F., Woolrich, M.W.: Probabilistic diffusion tractography with multiple fibre orientations: What can we gain? *NeuroImage* **34**(1), 144–55 (2007)
10. Hosey, T., Williams, G., Ansoerge, R.: Inference of multiple fiber orientations in high angular resolution diffusion imaging. *Magn. Reson. Med.* **54**, 1480–1489 (2005)
11. Rao, M., Chen, Y., Vemuri, B.C., Wang, F.: Cumulative residual entropy: a new measure of information. *IEEE Trans. Inf. Theory* **50**(6), 1220–1228 (2004)
12. Chen, Y., Guo, W., Zeng, Q., Yan, X., Rao, M., Liu, Y.: Apparent diffusion coefficient approximation and diffusion anisotropy characterization in DWI. In: *Information Processing in Medical Imaging*, Glenwood Springs, *MICCAI*, Berlin/New York, pp. 246–257. Springer, Berlin/New York (2005)
13. Descoteaux, M., Angelino, E., Fitzgibbons, S., Deriche, R.: Apparent diffusion coefficients from high angular resolution diffusion imaging: estimation and applications. *Magn. Reson. Med.* **56**, 395–410 (2006)
14. Özarslan, E., Vemuri, B.C., Mareci, T.H.: Generalized scalar measures for diffusion MRI using trace, variance, and entropy. *Magn. Reson. Med.* **53**(4), 866–76 (2005)
15. Leow, A., Zhu, S., Zhan, L., McMahon, K., de Zubicaray, G., Meredith, M., Wright, M., Thompson, P.: A study of information gain in high angular resolution diffusion imaging (HARDI). In: *Computational Diffusion MRI Workshop*, *MICCAI*, Berlin/New York, pp. 97–105 (2008). <http://picsl.upenn.edu/cdmri08/proceedings.pdf>
16. Prčkovska, V., Vilanova, A., Poupon, C., Haar Romeny, B.M., Descoteaux, M.: Fast classification scheme for hardi data simplification. In: Davcev, D., Gómez, J.M. (eds.) *ICT Innovations 2009*, Ohrid, pp. 345–355. Springer, Berlin/Heidelberg (2010)
17. Poupon, C., Rieul, B., Kezele, I., Perrin, M., Poupon, F., Mangin, J.F.: New diffusion phantoms dedicated to the study and validation of HARDI models. *Magn. Reson. Med.* **60** (2008) 1276–1283
18. Jones, D., Horsfield, M., Simmons, A.: Optimal strategies for measuring diffusion in anisotropic systems by magnetic resonance imaging. *Magn. Reson. Med.* **42**, 515–525 (1999)
19. Descoteaux, M., Angelino, E., Fitzgibbons, S., Deriche, R.: Regularized, fast and robust analytical q-ball imaging. *Magn. Reson. Med.* **58**, 497–510 (2007)
20. Wedeen, V.J., Hagmann, P., Tseng, W.Y., Reese, T.G., Weisskoff, R.M.: Mapping complex tissue architecture with diffusion spectrum magnetic resonance imaging. *Magn. Reson. Med.* **54**(6), 1377–1386 (2005)
21. Westin, C.F., Peled, S., Gudbjartsson, H., Kikinis, R., Jolesz, F.A.: Geometrical diffusion measures for MRI from tensor basis analysis. In: *ISMRM '97*, Vancouver, p. 1742 (1997)
22. Vilanova, A., Zhang, S., Kindlmann, G., Laidlaw, D.: An introduction to visualization of diffusion tensor imaging and its applications. In: Weickert, J., Hagen, H. (eds.) *Visualization and Processing of Tensor Fields*. Mathematics and Visualization, pp. 121–153 Springer, Berlin/Heidelberg/New York (2005)

23. Fawcett, T.: An introduction to roc analysis. *Pattern Recognit. Lett.* **27**(8), 861–874 (2006).  
ROC Analysis in Pattern Recognition
24. Prčkovska, V., Roebroek, A.F., Pullens, W., Vilanova, A., ter Haar Romeny, B.M.: Optimal acquisition schemes in high angular resolution diffusion weighted imaging. In: *MICCAI, Berlin/New York. Lecture Notes in Computer Science*, vol. 5242, pp. 9–17. Springer, Berlin/New York (2008)
25. Jansons, K.M., Alexander, D.: Persistent angular structure: new insights from diffusion magnetic resonance imaging data. *Inverse Probl.* **19**, 1031–1046 (2003)
26. Schnell, S., Saur, D., Kreher, B., Hennig, J., Burkhardt, H., Kiselev, V.: Fully automated classification of HARDI in vivo data using a support vector machine. *NeuroImage* **46**(3), 642–651 (2009)